Research Article Vol. 33, No. 4 / 24 Feb 2025 / *Optics Express* 8971

Optics EXPRESS

Dynamically reconfigurable 2D polarization-agnostic image edge-detection using nonvolatile phase-change metasurfaces

STUART KENDALL,[1] CARLOTA RUIZ DE GALARRETA,[1,2] JOE SHIELDS,[1] JACOPO BERTOLOTTI,[1] GUOCE YANG,[3] MENGYUN WANG,[3] ANDREA ALÙ,[4] HARISH BHASKARAN,[3] AND C. DAVID WRIGHT[1,*]

[1] *Centre for Metamaterials Research and Innovation, University of Exeter, Exeter EX4 QF, United Kingdom*
[2] *Institute of Materials Science of Barcelona (ICMAB-CSIC), Campus de la UAB, Bellaterra 08193, Spain*
[3] *Department of Materials, University of Oxford, Parks Road, Oxford OX1 3PH, United Kingdom*
[4] *Photonics Initiative, Advanced Science Research Center, City University of New York, New York, NY, USA*
[*] *david.wright@exeter.ac.uk*

Abstract: The development of novel, compact, and reconfigurable devices for optical analog computing would pave the way for the next generation of imaging systems free from high power consumption electronics and computationally demanding processing algorithms. Recently, nonlocal metasurfaces have emerged as a powerful platform to perform analog image processing operations with low energy consumption, at the speed of light, and without the need to physically access the Fourier space, thereby providing both high computational speeds and ease of integration. However, once such devices are designed and fabricated, their effect on optical beams is fixed, constraining their performance to a singular function. Here, we show how nonlocal metasurfaces made of novel low-loss chalcogenide phase-change materials, such as Sb_2Se_3, offer a degree of reconfigurability, enabling switching between certain imaging modes. Specifically, we show that switching between a two-dimensional edge-detection mode and a bright-field imaging mode, or between a two-dimensional edge-detection mode and a two-dimensional image blurring mode, is possible.

Published by Optica Publishing Group under the terms of the Creative Commons Attribution 4.0 License. Further distribution of this work must maintain attribution to the author(s) and the published article's title, journal citation, and DOI.

1. Introduction

In the era of big data and artificial intelligence, computing capabilities offered by conventional digital methods face performance challenges when compared to the massive scaling of computational needs. As a result, scientific efforts are currently being redirected towards the development of novel, faster, energy efficient, and compact analog signal processing and computing devices [1–4]. In this context, nonlocal metasurfaces - whose meta-atoms tailor the input wave collectively and result in a real-space invariant but momentum-space variant response and can directly modulate the Fourier component of light fields - have emerged as a promising all-optical analog alternative to traditional, electronically based signal processing techniques [1,5,6]. The reason for this lies in the ability to engineer nonlocal metasurface optical transfer functions in momentum space (i.e., engineer their dispersion characteristics), allowing them to be utilized for direct signal processing of optical beams, so carrying out important computing functions, such as convolution, in a massively parallel fashion. [7]. Therefore, nonlocal metasurfaces can perform computational tasks on signals, such as images, in a pure analog fashion at the speed of light, while avoiding the need of *i*) physically accessing the Fourier plane (which usually requires the use of bulky 4f lens systems) [8]; and *ii*) high energy consumption and long processing times arising from

#543602 https://doi.org/10.1364/OE.543602
Journal © 2025 Received 28 Nov 2024; revised 9 Feb 2025; accepted 9 Feb 2025; published 21 Feb 2025

computationally demanding serial (or parallel-limited) processing algorithms [1,5,6]. Moreover, the high operational speeds and ability to offer precise control of various optical analog operations of nonlocal metasurfaces are attractive for a variety of cutting edge technologies, including computer vision, medical imaging or augmented reality, to name but a few. As a result, in recent years a variety of nonlocal metasurface approaches have emerged with the aim of implementing analog image processing tasks. In particular, significant attention has been focused on image edge-detection, often the first step in object identification and classification tasks and enabled through first, second, and even higher-order spatial differentiation on an input image [7,9–12].

Although several previous metasurface designs have proven capable of performing image edge-detection [7,9–12], these are generally static, and therefore limited to a single functionality once fabricated. The ability to achieve multiple functionalities in a single analog computing metasurface would pave the way for significantly more versatility, thereby proving extremely useful for real world applications. One possible way of implementing multi-functionality is through the use of chalcogenide phase-change materials (PCMs) in combination with metasurface architectures, the approach we adopt here.

Traditionally employed in nonvolatile optical and electronic memories, PCMs are material alloys that can be switched between amorphous, crystalline, and intermediate (i.e., mixed) states by means of heat stimuli, which can be supplied in the form of either electrical or optical excitation [13,14]. The amorphous to crystalline transition is achieved via heating the material above its crystallisation temperature, typically of the order of 150 to 350 °C, depending on the composition. Amorphisation is achieved by melting of the alloy (usually between 500 and 700 °C, again depending on composition), followed by a rapid cooling (melt quenching) to prevent re-crystallisation of the material and so provide access to the less energetically favourable amorphous state. Such switching processes typically take place on timescales ranging from a few hundred picoseconds in nanoscale memory type devices, to the microsecond to many milliseconds range when switching metasurface devices by in-situ methods such as via the use of embedded micro-heaters, depending on material composition and specific device structure [13–15]. Moreover, such switching can be repeated many times, with a cycling endurance (i.e., number of successful switching cycles) of over 10 million having recently been reported for Sb_2Se_3 films of similar thicknesses to those reported here [15]. Perhaps more importantly, chalcogenide phase-change materials are nonvolatile in nature, meaning that a particular solid state can remain stable at room temperature for years without the need for a constant heat stimulus [13], making them good candidates for low power consumption applications.

As a result of the excellent properties offered by PCMs, over the past decade a variety of reconfigurable phase-change metasurfaces and metadevices have been demonstrated [16,17]. Examples include dynamic beam steering [18–20], reconfigurable lensing [21–23], and active absorbers and modulators [24–27] to mention a few. Moreover, albeit traditional PCMs such as GeSbTe and GeTe alloys are inherently lossy in at least one of their structural phases [28], the recent development of wider band gap, low-loss PCMs incorporating selenium (e.g., GeSbSeTe, SbSe) [28,29], or sulphur (SbS, GeSbTeS) [29,30] is opening up a new range of possibilities in the field of reconfigurable nanophotonic devices operating at near-infrared and visible wavelengths [17,20–22,26,31,32].

In this work, therefore, we present the design and analysis of high efficiency phase-change nonlocal metasurfaces capable of performing reconfigurable image processing tasks in the near-infrared, employing the novel low-loss material Sb_2Se_3. As depicted in Fig. 1(a), our metasurface can perform image edge-detection operations when the Sb_2Se_3 material is in its crystalline state. This is achieved by optimizing the structure so as to apply a Laplacian-like (second order differentiation) transfer function to impinging beams, thereby blocking small incident angles θ corresponding to low spatial frequencies. After switching to the amorphous phase, however, our device imposes a pass-through transfer function, resulting in bright-field imaging (Fig. 1(b)). The same basic metasurface design, with a suitable re-scaling of the unit cell dimensions, can also provide a dual image blurring/edge-detection functionality, a point to which we return in Sec. 2.3. Finally, our designs can perform such operations for numerical apertures (NA) as high as 0.5 ($\theta = \pm 30°$), in two dimensions, and independently of the incident beam polarization; properties which are well-suited for real world applications. Our findings pave the way to all-optical, compact, solid-state and reconfigurable analog image processing devices employing chalcogenide phase-change materials.

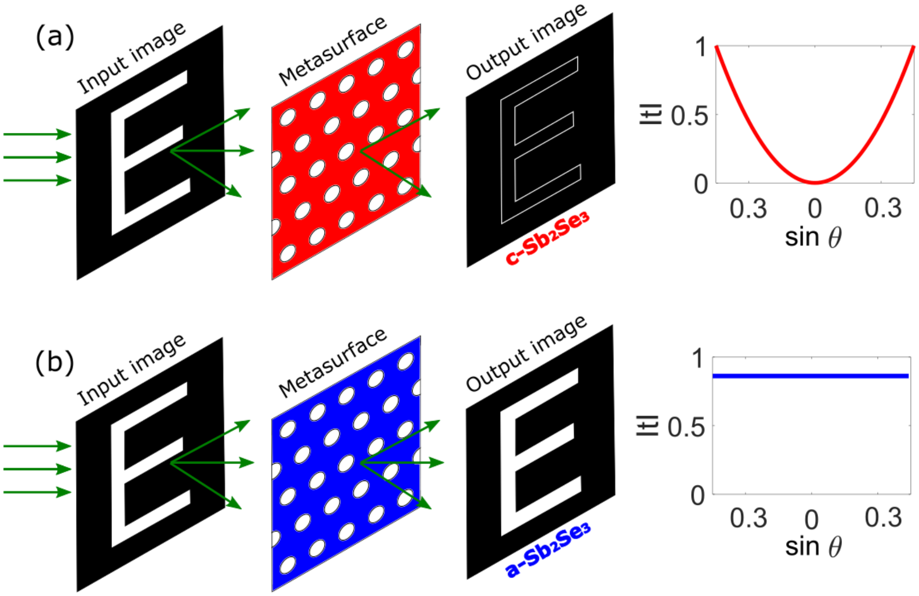

Fig. 1. Working principle of our nonlocal metasurfaces for reconfigurable image edge-detection. (a) When the Sb_2Se_3 metasurface is in its crystalline state, a Laplacian transfer function is imposed to impinging beams, resulting in low spatial frequencies or elevation angles being restricted, thereby imposing the desired edge-detection functionality to the input image. (b) After switching to the amorphous state, the transfer function becomes flat (i.e., non-dispersive), resulting in bright field imaging.

2. Results and discussion

2.1. Metasurface design framework

Edge-detection can be understood in terms of the high pass filtering of the spatial frequency content of an image, thereby enhancing its fine details while diminishing unwanted low spatial frequency information. Traditionally, this can be performed via the use of bulky $4f$ spatial filter systems consisting of a pair of lenses (typically of equal focal length f), separated by a distance of $2f$. In such a setup, spatial frequencies of an input image are decomposed and mapped in momentum space at the focal plane of the first lens. Here, one can physically filter out the low spatial frequencies using an amplitude aperture preventing transmission of low spatial frequencies, and then the second lens performs an inverse Fourier transform in order to reconstruct the edge-enhanced image [8]. The same effect can be performed computationally, via the use of Laplacian (∇^2) convolution masks applied to digital images [33]. Here we use an optical equivalent of this approach, applying an optical Laplacian-like convolution mask using a nonlocal metasurface. This removes the need to physically access the Fourier plane, as required in the $4f$ optical system, significantly improving the compactness and integratability of the design.

As stated in the introduction, nonlocal metasurfaces imposing on-demand Laplacian-like transfer functions to optical beams have been recently proven to offer compactness, while taking advantage of the high speed and low energy consumption of 4f optical systems [7,9,12]. The working principle of such nonlocal metasurfaces is represented in Fig. 2(a). We first consider an input image incident upon the metasurface, having an intensity profile of the form $I_{in}(x, y) = | \boldsymbol{E}_{in}(x, y) |^2$ where $\boldsymbol{E}_{in}(x, y) = E_{in}(x, y)\boldsymbol{e}$ is the complex electric field (whose angular frequency ω is $\omega = 2\pi/\lambda_0 = ck_0$), and $\boldsymbol{e}$ being the direction of polarization. The beam emerging from the input image can be decomposed into a series of discrete plane waves, whose directions can be fully defined in polar coordinates by the elevation (θ) and azimuth (ϕ) angles. After interacting with the metasurface, the amplitude of the output electric field E_{out} will be proportional to its Fourier transform f_{out}, following:

$$f_{out} = t(k_x, k_y) \int e^{-i(k_x x + k_y y)} E_{in}(x, y) dxdy \tag{1}$$

where $t(k_x, k_y)$ is the transfer function of the metasurface, with $[k_x, k_y]$ being related to the θ and ϕ angles by $[k_x, k_y] = k_0 sin\theta[cos\phi, sin\phi]$. Therefore, on-demand mathematical operations defined in the frequency domain can be performed in real space, by optimizing the transfer function of the metasurface $t(k_x, k_y)$ (corresponding to $t(\theta, \phi)$). In particular, for a Laplacian-like edge-detection operation, such a transfer function should satisfy a parabola defined by the second order differentiation $t = -(k_x^2 + k_y^2)$.

The schematics and unit cell of our metasurface design platform employed for reconfigurable 2D image edge-detection are presented in Fig. 2(b). The design consists of a Sb_2Se_3 film with a regular hexagonal array of cylindrical holes on a SiO_2 substrate. The entire geometry can be defined by three key parameters, namely the period Λ, the hole diameter D, and the Sb_2Se_3 layer thickness h. We choose to use Sb_2Se_3 due to its outstanding optical properties (i.e., complex refractive index) in the near-infrared [23,29,34]. In particular, as shown in Fig. 2(c), Sb_2Se_3 possesses high transparency in the near-infrared spectral regime (with k= 0 for both amorphous and crystalline states), while maintaining a high contrast between phases in n of around $\Delta n = 0.7$ at the telecommunication band of interest to this work (i.e., the C-band corresponding to a $\lambda = 1530$ nm to $\lambda = 1565$ nm spectral region). For a 2D, polarization insensitive performance, the modulus of the metasurface transfer functions should be axisymmetric in k-space, and identical for parallel and sagittal co-polarizations (namely $|t_{pp}|$ and $|t_{ss}|$ respectively). Moreover, its cross-polarized transfer functions should be ideally minimized to $|t_{ps}| = |t_{sp}| = 0$. Taking this into account, our metasurface design was optimized to satisfy two conditions simultaneously:

- A Laplacian transfer function when the Sb_2Se_3 is crystalline, resulting in an edge-detection functionality following:

$$\begin{bmatrix} |t_{pp}|(k_x, k_y) & |t_{sp}|(k_x, k_y) \\ |t_{ps}|(k_x, k_y) & |t_{ss}|(k_x, k_y) \end{bmatrix} = \begin{bmatrix} k_x^2 + k_y^2 & 0 \\ 0 & k_x^2 + k_y^2 \end{bmatrix} \tag{2}$$

- A flat and constant transfer function when the metasurface switches to the amorphous state, which would provide the bright-field imaging capability:

$$\begin{bmatrix} |t_{pp}|(k_x, k_y) & |t_{sp}|(k_x, k_y) \\ |t_{ps}|(k_x, k_y) & |t_{ss}|(k_x, k_y) \end{bmatrix} = \begin{bmatrix} 1 & 0 \\ 0 & 1 \end{bmatrix} \tag{3}$$

The geometrical parameters to provide an optimum compromise between both conditions were found to be $\Lambda = 836$ nm, $D = 479$ nm and $h = 250$ nm. Note that assigning the crystalline state

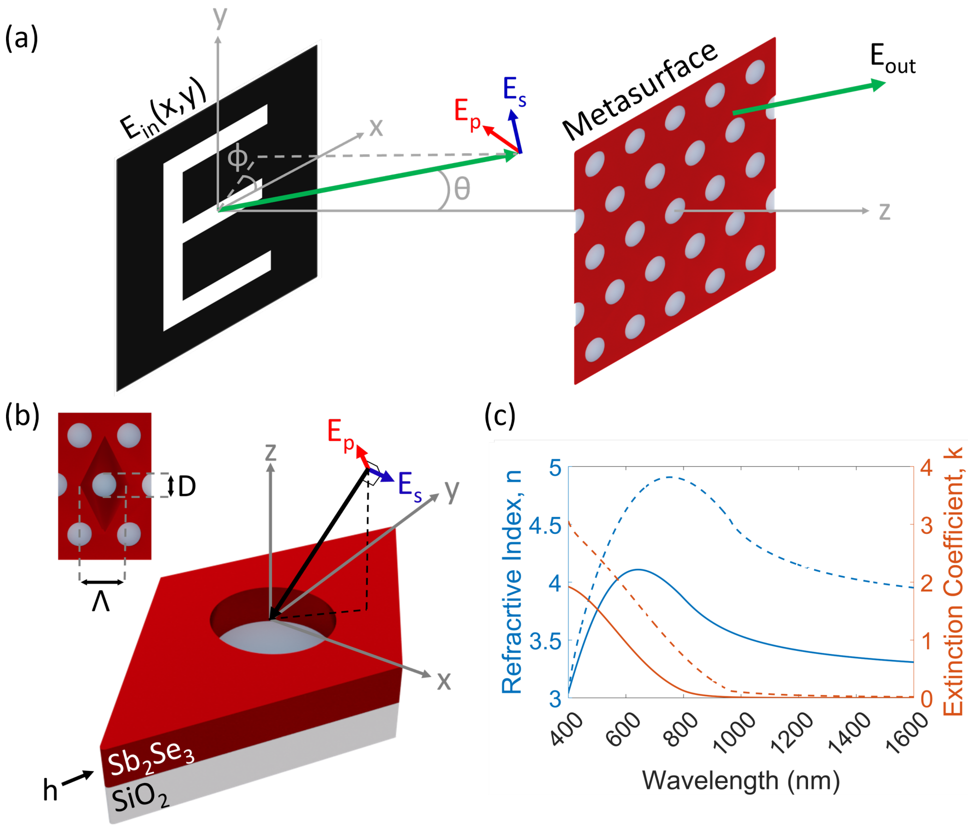

Fig. 2. (a) Diagram showing input fields scattered by the image, and subsequently filtered by the metasurface. (b) Schematics of the phase-change nonlocal metasurface presented in this work, showing geometrical details and materials of the unit cell. (c) Refractive index (blue) and extinction coefficient (red) of amorphous (solid lines) and crystalline (dashed lines) Sb_2Se_3, extracted from [23].

as the edge-detection mode is due to its characteristic higher refractive index. Such functionality requires excitation of leaky guided mode resonances following the above-mentioned dispersion characteristics in k-space. Upon amorphization, such resonances are shifted towards shorter wavelengths due to a decrease in refractive index (see Fig. 2(c)), providing the desired off-resonant, dispersionless behaviour required for a bright field functionality at the desired wavelengths.

The resulting absolute co-polarized transfer functions for various polarization states are depicted in Fig. 3, over a range of normalized spatial frequencies $[k_x/k_0, k_y/k_0] = \pm 0.5$ (corresponding to an elevation angle range of ±30 ° and a numerical aperture of 0.5). Figures 3(a)-(c) show the co-polarized transfer functions for parallel polarization (p-pol), sagittal polarization (s-pol) and right circular polarization (rcp) respectively when the Sb_2Se_3 is in its crystalline state. Overall, when the metasurface is in the crystalline phase, all polarization states exhibit blocking of low spatial frequencies, as required by image edge-detection. More specifically, as it can be seen in Fig. 3(a), the transfer function of p-polarized beams shows a good approximation to Laplacian profile (defined by Eq. (2)), with close to zero transmission at $[k_x, k_y] = [0, 0]$ increasing radially in a parabolic-like fashion towards the limits of k-space. For s-pol (Fig. 3(b)), we find an similar behaviour, however, the transmission coefficient is here less good when compared to the p-pol state due to the presence of annular dips taking place at intermediate values of $[k_x, k_y]$. As we will show in the next section, such features were found to have negligible effects on the final processed images. Finally, in Fig. 3(c) we show the transmission response for right circular (rcp) polarization, which, as would be expected, is found to possess features from both p- and s-polarizations, offering a good compromise between both performances.

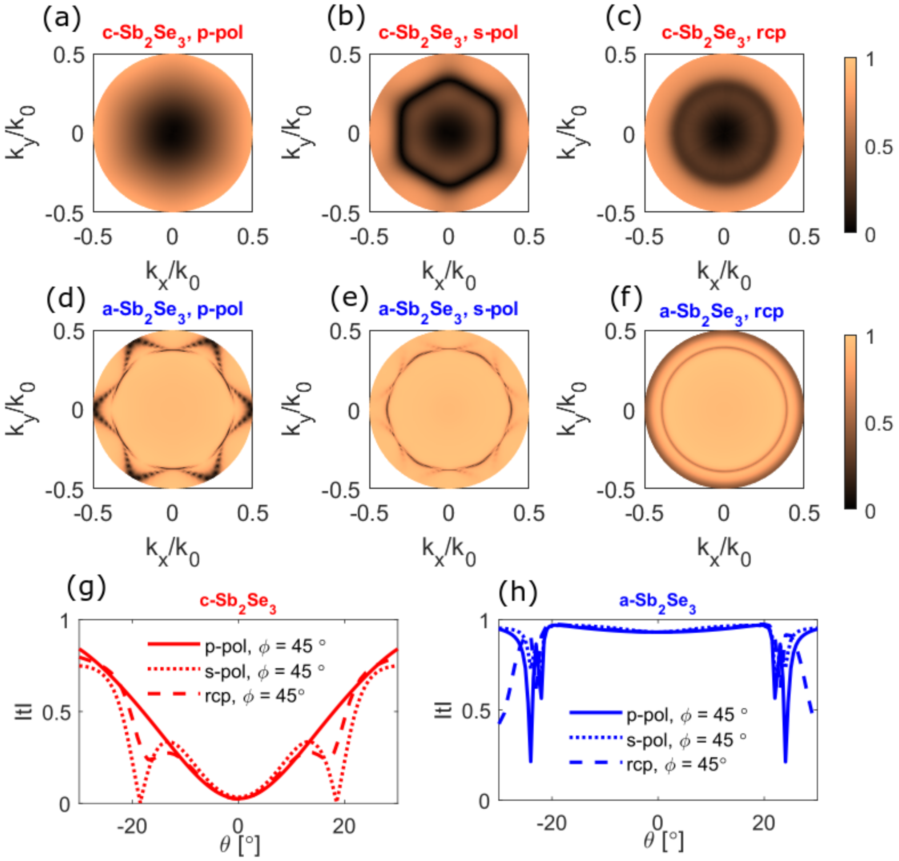

Fig. 3. Absolute co-polarized transfer functions ($|t|(k_x/k_0, k_y/k_0)$) of the optimized metasurface for a wavelength of $\lambda = 1540$ nm. (a)-(c) Crystalline state response for: (a) p-pol, (b) s-pol and, (c) rcp. (d)-(f) Amorphous state response for: (d) p-pol, (e) s-pol and, (f) rcp. (g),(h) Cross sections of the transmission coefficients of all the polarization states, for $\phi = 45°$: (g) crystalline state, (h) amorphous state.

The other intended purpose for our device presented here is reconfigurability to a bright-field imaging mode when the Sb_2Se_3 is switched from its crystalline state to its amorphous state. In Figs. 3(d)-(f), we show the co-polarized transfer functions, again for p-pol, s-pol and rcp cases respectively. Overall, it can be seen that all the polarization states match the required transfer functions for bright-field imaging, consisting of high and constant transmission values along k-space, as defined by Eq. (3). We do however note that some dips in transmission occur at the higher $[k_x/k_0, k_y/k_0]$, but this would cause the blocking of some specific high spatial frequencies only, due to the sharp nature of the dips.

Finally, for clarity, in Figs. 3(g) and (h), we show the cross sections of the absolute transmission for all incident polarizations as a function of θ, for an azimuth angle of $\phi = 45$ °. Indeed, Fig. 3(g) confirms Laplacian-like profiles with zero transmission values at $\theta = 0$ ° for all the polarization states when the metasurface is crystalline, with a slightly better performance occurring for p-pol.

In Fig. 3(h), the amorphous phase reveals very high (near unity) and almost constant transmission values for all the polarization states, though with the characteristic sharp dips at large elevation angles (corresponding to high $[k_x/k_0, k_y/k_0]$ values) discussed previously.

2.2. *Reconfigurable imaging capabilities*

We demonstrate the functionality of our reconfigurable edge-detection/bright-field imaging device through the simulation of the metasurface acting upon an input image of the letter E, shown in Fig. 4(a) and (i). The input test image has an intensity of 1 to contrast the background of 0 intensity, and has an overall size of 500 by 500 pixels. The edges of the input image extend over a region of 4 pixels. The imaging performance is evaluated by its responses to both horizontal and vertical linearly polarized light as well as rcp light.

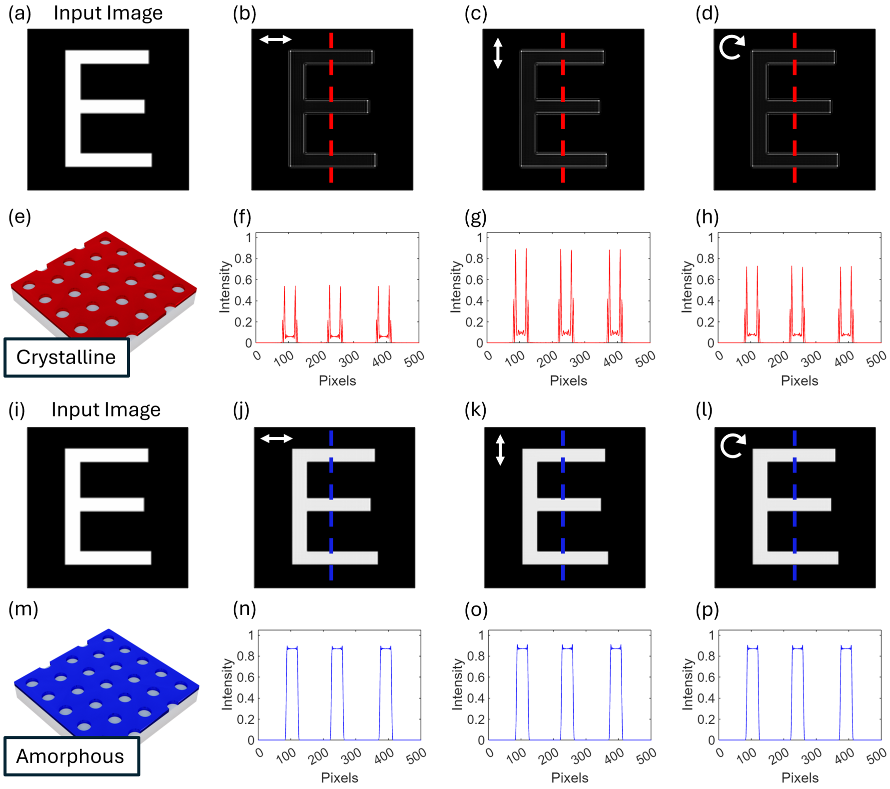

Fig. 4. (a) Input image for testing the functionality of the device in its crystalline state. (b)-(d) Device simulation results for edge-detection for the cases of horizontal and vertical linear polarization and rcp, respectively. (e) Crystalline device unit cell array schematic. (f)-(h) Vertical cross-sections of the device functionalities for the cases of horizontal polarization, vertical polarization and rcp, respectively. (i) Input image for testing the functionality of the device in its amorphous state. (j)-(l) Device simulation results for bright-field imaging for the cases of horizontal and vertical linear polarization and rcp, respectively. (m) Amorphous device unit cell array schematic. (n)-(p) Vertical cross-sections of the device functionalities for the cases of horizontal polarization, vertical polarization and rcp, respectively.

Figures 4(b)-(d) show the simulated outputs of the crystalline metasurface (shown schematically in Fig. 4(e)) for horizontally polarized, vertically polarized and rcp light, respectively, with red dashed lines indicating the cross-sections used for the graphs shown below in Figs. 4(f)-(h). The cross-sections show clearly the edge-detection functionality of the device, with the edge of the input image clearly highlighted with two sharp peaks that match the positions of the edges shown in the input image cross-section (note that the edge-detection cross-section profiles have a scale factor of 100 in the y-axis). Furthermore, the intensity between the pairs of peaks within the edge-detection profile are very low and there are minimal fringes in the output image. Adopting a definition of peak and average edge-detection efficiencies given by Cotrufo et al. [7], we obtain values of 8% - 9% and 1.2% - 1.4% respectively, very close to those of an ideal Laplacian edge-detector (see [7] for more details).

Simulation of the functionality of the metasurface in its amorphous state is shown, again with an input image of the letter E, in Fig. 4. Figures 4(j)-(l) show the simulated outputs of the amorphous metasurface for horizontally polarized, vertically polarized and rcp light, respectively, with blue dashed lines to indicate the cross-sections used for the graphs shown in Figs. 4(n)-(p). The cross-sections show that the intensity profiles match that of the input image and that there are minimal fringes within the image for all cases. These profiles all have a scale factor of 1. Figure 4(m) displays a schematic of the amorphous unit cell array.

The metasurface presented above can also be tailored to enable a dual edge-detection/image blurring functionality, demonstrating the inherent versatility of our design. Image blurring reduces the high frequency content of an image and is often used as a pre-processing step in computer vision and image processing (e.g., reducing the high-frequency content can help to identify objects of interest by emphasising an image's larger structural features). Our blurring device maintains the previous structure of a Sb_2Se_3 film with a regular hexagonal lattice array of cylindrical holes on a SiO_2 substrate, but with the unit cell parameters scaled in size to $\Lambda = 684$ nm, $D = 392$ nm and $h = 207.5$ nm. This re-scaled design performs, at a wavelength $\lambda = 1110$ nm, edge-detection in the amorphous phase and image blurring in the crystalline phase. Image blurring is achieved via a low-pass filter type response, allowing for high transmission at lower spatial frequencies, whilst filtering out the higher spatial frequency components.

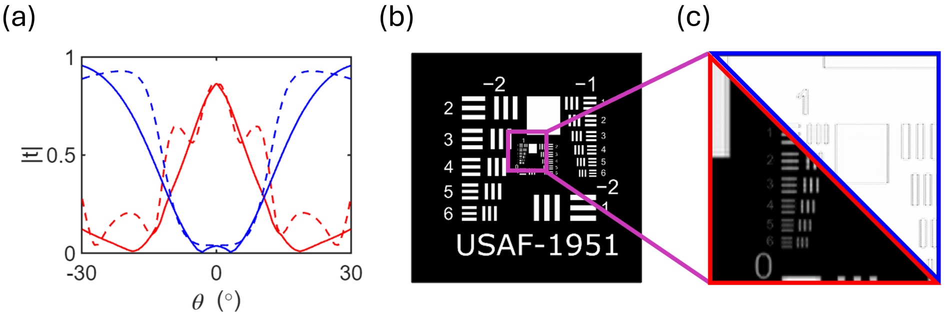

Fig. 5. Device transmission response and functionality simulation for an edge-detection/blurring dual-functionality device at a wavelength of $\lambda = 1110$ nm. (a) Transmission responses for the device in both its crystalline state for image blurring (red) and its amorphous state for edge-detection (blue), with s-pol and p-pol responses displayed via dashed and solid lines, respectively. (b) Input image (USAF-1951 test target) for evaluating the imaging capabilities of the device. (c) Simulation results of both the crystalline blurring mode (red) and the amorphous edge-detection mode (blue) shown for horizontal input polarization (edge-detection mode output is inverted for clarity).

The edge-detection/image blurring device performance is shown in Fig. 5. Figure 5(a) displays the transmission response in both amorphous (blue lines) and crystalline (red lines) states for both s and p input polarizations (and up to ±30 ° incident angle). The requisite Laplacian and low-pass type responses for edge-detection and image blurring are clearly obtained, again with polarization independence over the same range of incident angles as for our previous design. Figure 5(b) shows a USAF-1951 test target which is used as the input image for the testing of the device functionality. Figure 5(c) shows the output of the image blurring mode (red) and the edge-detection mode (blue) of the device for a horizontal input polarization. The blurring mode of the device is effective as the larger image features are blurred and the smaller, sharper features are almost no longer visible as expected. The performance of the edge-detection mode, as with the previous design, show that the edges are clearly visible. Note that the output is inverted for clarity.

Finally, we note that although the transfer functions of the above designed metasurfaces will be affected by fabrication tolerances that potentially result in the precise values for the target geometric parameters (of period, Λ, hole diameter, d, and the Sb_2Se_3 layer thickness, h) not being achieved, we found that changes resulting from a simultaneous variation of +/- 2 nm in all such parameters could be readily alleviated by a small (few nanometer) change in the operating wavelength.

3. Conclusions

We have presented and theoretically demonstrated a design for a polarization independent reconfigurable phase-change metasurface with dual edge-detection and bright-field imaging capability. It has been shown that for an operational wavelength of 1540 nm, our metasurface design exhibits Laplacian-like dispersion characteristics needed for edge-detection up to high NA (up to NA = 0.5) values when in its crystalline state. In the amorphous state the metasurface has a high transmission amplitude across the NA range, yielding a bright-field imaging mode. The dispersion characteristics displayed in both material phase states are consistent for s-pol, p-pol and rcp incident light ensuring that the device performance is both polarization independent and 2D in application. We demonstrated the dual functionality capabilities of our design via the simulation of a 2D image incident upon the metasurface for each of the three polarization cases, with the results showing the desired functionality and good efficiency for both modes (edge-detection and bright-field mode). The same basic metasurface design can also be re-scaled in size to provide a dual functionality of edge-detection and image blurring, here at a wavelength of 1110 nm. This version of the design maintains the Laplacian-like dispersion characteristics needed for edge-detection up to NA = 0.5, although now in the amorphous phase state, with the crystalline state displaying low-pass filter type dispersion characteristics needed for image blurring. Again, this device is both polarization independent and 2D in application.

The results presented here show that a level of multi-functionality can be implemented into metasurface devices designed for analog optical computing via the integration of phase-change materials. This capability is achieved here through a relatively simple design, and as such fabrication of such multi-purpose devices is eminently feasible. Future designs should be able to take advantage of other combinations of potentially more complex functionalities, through more complex dispersion characteristics as well as possibly more reconfigurability via the use of intermediate phase-change states.

4. Appendix: Calculation of the image processing capabilities of PCM-based nonlocal metasurfaces

We provide insight into the mathematical framework employed to determine the image processing capabilities of our metasurfaces, based on their $[k_x/k_0, k_y/k_0]$ transfer matrices calculated via COMSOL. Such a framework was employed for all the metasurface functionalities discussed in the main paper, namely edge-detection, bright-field imaging and image blurring.

The optical response of our metasurfaces was first numerically calculated via COMSOL, in order to obtain the sagittal, parallel, and right circularly polarized (s-pol, p-pol and rcp) transfer matrices containing the complex transmission amplitudes for each metasurface functionality (namely transmission coefficient and optical phase). Such matrices were calculated for a range of elevation and azimuth angles to ensure both 2D functionality and polarization independence. The elevation angle θ was swept from 0° to 30°, whereas azimuth angle ϕ was swept from 0° to 360°. This corresponds to an effective numerical aperture (NA) of 0.5, and thus a normalized spatial frequency range of $[k_x/k_0, k_y/k_0] = \pm 0.5$.

Then, the image processing capabilities of our metasurfaces were investigated by first taking the intensity profile of the incident input electric field (input image), $\mathbf{I}_{in}(x, y) = |\mathbf{E}_{in}(x, y)|^2$, where $\mathbf{E}_{in}(x, y)$ is the input electric field. On the other hand, the input electric field polarization at normal incidence can be defined via the unit vector $\mathbf{p}$ along the x- and y- axes, such that the polarized electric field input becomes $E_{in}(x, y)\mathbf{p}$ in real space. This gives an input electric field polarization vector of $\mathbf{p} = (1, 0, 0)$, and $\mathbf{p} = (0, 1, 0)$, for x- (horizontal) and y- (vertical) polarizations respectively. The Fourier transform of the electric field, $f_{in}(k_x, k_y)$, can be then used to describe the field in k-space such that the input becomes $f_{in}(k_x, k_y)\mathbf{q}(k_x, k_y)$, where $\mathbf{q}(k_x, k_y) = (\mathbf{k} \times \mathbf{p}) \times \mathbf{k}/|\mathbf{k}|$ with $\mathbf{k}$ being the k-vector. The s-pol and p-pol components of the electric field become $E_s(k_x, k_y) = f_{in}(k_x, k_y)\mathbf{q}(k_x, k_y) \cdot \mathbf{e}_s$ and $E_p(k_x, k_y) = f_{in}(k_x, k_y)\mathbf{q}(k_x, k_y) \cdot \mathbf{e}_p$, where $\mathbf{e}_s = \mathbf{k} \times \mathbf{z}/|\mathbf{k}|$ and $\mathbf{e}_p = \mathbf{k} \times \mathbf{e}_s/|\mathbf{k}|$, with $\mathbf{z}$ being the unit vector in the z direction. The metasurface transfer function in k-space has the form:

$$t(k_x, k_y) = \begin{pmatrix} \mathbf{e}_p & \mathbf{e}_s \end{pmatrix} \begin{pmatrix} t_{pp}(k_x, k_y) & t_{ps}(k_x, k_y) \\ t_{sp}(k_x, k_y) & t_{ss}(k_x, k_y) \end{pmatrix} \tag{4}$$

where $t_{pp}(k_x, k_y)$, $t_{ps}(k_x, k_y)$, $t_{sp}(k_x, k_y)$ and $t_{ss}(k_x, k_y)$ are the transfer function co- and cross-polarized components of the metasurface whose the subscripts denote the input and output polarized light. Taking $t_{ps}(k_x, k_y)$, for example, this would correspond to the transfer function between p-pol input light and s-pol output light. For all our metasurfaces, the cross polarization transmission coefficients $t_{ps}(k_x, k_y)$ and $t_{sp}(k_x, k_y)$ have near-zero values (i.e., below 3%), and therefore we assumed within these calculations to be zero.

Finally, since the calculated transfer functions are complex and thus possess amplitude and phase components, we have:

$$\begin{aligned} t_{pp}(k_x, k_y) &= |t_{pp}(k_x, k_y)| e^{i\varphi_{pp}(k_x, k_y)} \quad \text{and} \\ t_{ss}(k_x, k_y) &= |t_{ss}(k_x, k_y)| e^{i\varphi_{ss}(k_x, k_y)} \end{aligned} \tag{5}$$

where $|t_{pp}(k_x, k_y)|$ and $|t_{ss}(k_x, k_y)|$ are the transmission coefficients through the metasurface for each case, and $\varphi_{pp}(k_x, k_y)$ and $\varphi_{ss}(k_x, k_y)$ is the optical phase.

Combining the terms for the input electric field and the metasurface transfer function, we can now define the output electric field in Fourier space $f_{out}(k_x, k_y)$:

$$f_{out}(k_x, k_y) = f_{in}(k_x, k_y) \cdot t(k_x, k_y) \begin{pmatrix} \mathbf{q} \cdot \mathbf{e}_p \\ \mathbf{q} \cdot \mathbf{e}_s \end{pmatrix} \tag{6}$$

which can be then inverse Fourier transformed to obtain the resulting final image, and thus evaluate the image processing capabilities of our metasurfaces.

Funding. Engineering and Physical Sciences Research Council (EP/W003341/1, EP/W022931/1); HORIZON EUROPE Marie Sklodowska-Curie Actions (10106808); Air Force Office of Scientific Research.

Acknowledgments. S.K., J.S., J.B., and C.D.W. acknowledge funding from the EPSRC A-META project (EP/W003341/1). H.B. and C.D.W. acknowledge funding from APT-NuCOM EPSRC project (EP/W022931/1). C.R. de G. acknowledges funding from the Marie Sklodowska-Curie Postdoctoral Fellowship 101068089 (METASCALE). A.A. was supported by the Air Force Office of Scientific Research.

Disclosures. The authors declare no conflicts of interest.

Data availability. Data relating to this paper can be obtained from the corresponding author by reasonable request.

References

1. D. Xu, S. Wen, and H. Luo, "Metasurface-based optical analog computing: From fundamentals to applications," Adv. Devices Instrum. **2022**, 0002 (2022).
2. A. Sebastian, M. Le Gallo, R. Khaddam-Aljameh, *et al.*, "Memory devices and applications for in-memory computing," Nat. Nanotechnol. **15**(7), 529–544 (2020).
3. J. Feldmann, N. Youngblood, M. Karpov, *et al.*, "Parallel convolutional processing using an integrated photonic tensor core," Nature **589**(7840), 52–58 (2021).
4. S. S. Gill, H. Wu, P. Patros, *et al.*, "Modern computing: Vision and challenges," Telematics Informatics Rep. **13**, 100116 (2024).
5. S. Abdollahramezani, O. Hemmatyar, and A. Adibi, "Meta-optics for spatial optical analog computing," Nanophotonics **9**(13), 4075–4095 (2020).
6. H. Zhou, C. Zhao, C. He, *et al.*, "Optical computing metasurfaces: applications and advances," Nanophotonics **13**(4), 419–441 (2024).
7. M. Cotrufo, A. Arora, S. Singh, *et al.*, "Dispersion engineered metasurfaces for broadband, high-na, high-efficiency, dual-polarization analog image processing," Nat. Commun. **14**(1), 7078 (2023).
8. J. W. Goodman, *Introduction to Fourier Optics* (Roberts and Company Publishers, 2005).
9. A. Cordaro, H. Kwon, D. Sounas, *et al.*, "High-index dielectric metasurfaces performing mathematical operations," Nano Lett. **19**(12), 8418–8423 (2019).
10. H. Kwon, A. Cordaro, D. Sounas, *et al.*, "Dual-polarization analog 2d image processing with nonlocal metasurfaces," ACS Photonics **7**(7), 1799–1805 (2020).
11. Y. Liu, M. Huang, Q. Chen, *et al.*, "Single planar photonic chip with tailored angular transmission for multiple-order analog spatial differentiator," Nat. Commun. **13**(1), 7944 (2022).
12. M. Cotrufo, S. Singh, A. Arora, *et al.*, "Polarization imaging and edge detection with image-processing metasurfaces," Optica **10**(10), 1331–1338 (2023).
13. M. Wuttig and N. Yamada, "Phase-change materials for rewriteable data storage," Nat. Mater. **6**(11), 824–832 (2007).
14. D. Wang, L. Zhao, S. Yu, *et al.*, "Non-volatile tunable optics by design: from chalcogenide phase-change materials to device structures," Mater. Today **68**, 334–355 (2023).
15. D. Lawson, S. Blundell, M. Ebert, *et al.*, "Optical switching beyond a million cycles of low-loss phase change material Sb_2Se_3," Opt. Mater. Express **14**(1), 22–38 (2024).
16. F. Ding, Y. Yang, and S. I. Bozhevolnyi, "Dynamic metasurfaces using phase-change chalcogenides," Adv. Opt. Mater. **7**(14), 1801709 (2019).
17. C. R. de Galarreta, S. G. Carrillo, Y. Au, *et al.*, "Tunable optical metasurfaces enabled by chalcogenide phase-change materials: from the visible to the THz," J. Opt. **22**(11), 114001 (2020).
18. C. R. de Galarreta, A. M. Alexeev, Y.-Y. Au, *et al.*, "Nonvolatile reconfigurable phase-change metadevices for beam steering in the near infrared," Adv. Funct. Mater. **28**(10), 1704993 (2018).
19. Y. Zhang, C. Fowler, J. Liang, *et al.*, "Electrically reconfigurable non-volatile metasurface using low-loss optical phase-change material," Nat. Nanotechnol. **16**(6), 661–666 (2021).
20. P. Moitra, Y. Wang, X. Liang, *et al.*, "Programmable wavefront control in the visible spectrum using low-loss chalcogenide phase-change metasurfaces," Adv. Mater. **35**(34), 2205367 (2023).
21. M. Y. Shalaginov, S. An, Y. Zhang, *et al.*, "Reconfigurable all-dielectric metalens with diffraction-limited performance," Nat. Commun. **12**(1), 1225 (2021).
22. G. Braid, C. Ruiz de Galarreta, A. Comley, *et al.*, "Optical and thermal design and analysis of phase-change metalenses for active numerical aperture control," Nanomaterials **12**(15), 2689 (2022).
23. M. Wang, J. S. Lee, S. Aggarwal, *et al.*, "Varifocal metalens using tunable and ultralow-loss dielectrics," Adv. Sci. **10**(6), 2204899 (2023).
24. A. Tittl, A.-K. U. Michel, M. Schäferling, *et al.*, "A switchable mid-infrared plasmonic perfect absorber with multispectral thermal imaging capability," Adv. Mater. **27**(31), 4597–4603 (2015).
25. S. G.-C. Carrillo, L. Trimby, Y.-Y. Au, *et al.*, "A nonvolatile phase-change metamaterial color display," Adv. Opt. Mater. **7**(18), 1801782 (2019).
26. C. R. de Galarreta, I. Sinev, A. M. Alexeev, *et al.*, "Reconfigurable multilevel control of hybrid all-dielectric phase-change metasurfaces," Optica **7**(5), 476–484 (2020).
27. J. Shields, C. R. De Galarreta, H. Penketh, *et al.*, "A route to ultra-fast amplitude-only spatial light modulation using phase-change materials," Adv. Opt. Mater. **11**(18), 2300765 (2023).
28. Y. Zhang, J. B. Chou, J. Li, *et al.*, "Broadband transparent optical phase change materials for high-performance nonvolatile photonics," Nat. Commun. **10**(1), 4279 (2019).
29. M. Delaney, I. Zeimpekis, D. Lawson, *et al.*, "A new family of ultralow loss reversible phase-change materials for photonic integrated circuits: Sb_2S_3 and Sb_2Se_3," Adv. Funct. Mater. **30**(36), 2002447 (2020).
30. Y. Miyatake, K. Makino, J. Tominaga, *et al.*, "Proposal of low-loss non-volatile mid-infrared optical phase shifter based on $Ge_2Sb_2Te_3S_2$," IEEE Trans. Electron Devices **70**(4), 2106–2112 (2023).

31. M. Delaney, I. Zeimpekis, H. Du, *et al.*, "Nonvolatile programmable silicon photonics using an ultralow-loss Sb_2Se_3 phase change material," Sci. Adv. **7**(25), eabg3500 (2021).
32. G. Yang, M. Wang, J. S. Lee, *et al.*, "Nonlocal phase-change metaoptics for reconfigurable nonvolatile image processing," arXiv (2024).
33. R. C. Gonzalez, *Digital Image Processing* (Pearson Education India, 2009).
34. W. Dong, H. Liu, J. K. Behera, *et al.*, "Wide bandgap phase change material tuned visible photonics," Adv. Funct. Mater. **29**(6), 1806181 (2019).

83.6.49.233 2026-02-13 05:15:08